



## Article

# The Surface Properties of Implant Materials by Deposition of High-Entropy Alloys (HEAs)

Khalid Usman <sup>1,†</sup>, Doori Kang <sup>1,†</sup>, Geonwoo Jeong <sup>1</sup>, Khurshed Alam <sup>1</sup>, Athira Raveendran <sup>1</sup>, Jinhui Ser <sup>1</sup>,  
Woohyung Jang <sup>2,\*</sup> and Hoonsung Cho <sup>1,\*</sup>

<sup>1</sup> School of Materials Science & Engineering, Chonnam National University, Gwangju 61186, Republic of Korea

<sup>2</sup> Department of Prosthodontics, School of Dentistry, Chonnam National University, Gwangju 61186, Republic of Korea

\* Correspondence: awj568@jnu.ac.kr (W.J.); cho.hoonsung@jnu.ac.kr (H.C.)

† These authors contributed equally to this work.

**Abstract:** High-entropy alloys (HEAs) contain more than five alloying elements in a composition range of 5–35% and with slight atomic size variation. Recent narrative studies on HEA thin films and their synthesis through deposition techniques such as sputtering have highlighted the need for determining the corrosion behaviors of such alloys used as biomaterials, for example, in implants. Coatings composed of biocompatible elements such as titanium, cobalt, chrome, nickel, and molybdenum at the nominal composition of  $\text{Co}_{30}\text{Cr}_{20}\text{Ni}_{20}\text{Mo}_{20}\text{Ti}_{10}$  were synthesized by means of high-vacuum radiofrequency magnetron (HVRF) sputtering. In scanning electron microscopy (SEM) analysis, the coating samples deposited with higher ion densities were thicker than those deposited with lower ion densities (thin films). The X-ray diffraction (XRD) results of the thin films heat treated at higher temperatures, i.e., 600 and 800 °C, revealed a low degree of crystallinity. In thicker coatings and samples without heat treatment, the XRD peaks were amorphous. The samples coated at lower ion densities, i.e.,  $20 \mu\text{Acm}^{-2}$ , and not subjected to heat treatment yielded superior results in terms of corrosion and biocompatibility among all the samples. Heat treatment at higher temperatures led to alloy oxidation, thus compromising the corrosion property of the deposited coatings.

**Keywords:** high-entropy alloys (HEAs); sputtering; corrosion; implants; biomaterial



**Citation:** Usman, K.; Kang, D.; Jeong, G.; Alam, K.; Raveendran, A.; Ser, J.; Jang, W.; Cho, H. The Surface Properties of Implant Materials by Deposition of High-Entropy Alloys (HEAs). *Nanomaterials* **2023**, *13*, 1123. <https://doi.org/10.3390/nano13061123>

Academic Editors: Maiyong Zhu and Jordi Sort

Received: 21 February 2023

Revised: 16 March 2023

Accepted: 19 March 2023

Published: 21 March 2023



**Copyright:** © 2023 by the authors. Licensee MDPI, Basel, Switzerland. This article is an open access article distributed under the terms and conditions of the Creative Commons Attribution (CC BY) license (<https://creativecommons.org/licenses/by/4.0/>).

## 1. Introduction

High-entropy alloys (HEAs) are emerging advanced materials, and they are also called multicomponent alloys, multi-principal-element alloys, and compositionally complex alloys (CCAs). These alloys were first reported in 2004 by two independent research groups, namely Yeh et al. [1] and Cantor et al. [2]. The alloy reported by the latter group was composed of an equimolar mixture of Cr, Mn, Fe, Co, and Ni (i.e., Cantor alloy [3]). Owing to the synergic property of HEAs, they appear to be a better alternative to existing biomaterials such as 316 L stainless steel, titanium, and its derivative alloys such as Ti 6Al 4V, as well as conventional alloys (CAs) such as ASTM F75, F90, and F562 (HS251-Haynes Stellite), also called Vitallium [4], in terms of corrosion and biocompatibility.

Over a broad temperature range, slow diffusion, lattice distortion, and high entropy are the defining characteristics of HEAs as compared to conventional alloys (CAs). The mixture of these properties affects the corrosion resistance, tribocorrosion, strength, hardness, ductility, wear, and erosion of HEAs [5]. HEAs have the potential for application in various industries, including aerospace, energy, refractory materials, and three-dimensional (3D) printing, in addition to their use as biomaterials in implants or surgical equipment.

The constituent materials of the  $\text{Co}_{30}\text{Cr}_{20}\text{Ni}_{20}\text{Mo}_{20}\text{Ti}_{10}$  HEA were selected from the perspective of biological compatibility. Co-Cr and its oxide states, e.g., Cr (VI), are considered CMR substances and cause lung cancer [6]. Ni sensitization is frequently accompanied by Co sensitization. There was no indication of Ti-specific hypersensitivity [7]. To ensure

the neoformation of tissues and organs and the cells in a scaffold, the surface must be compatible anatomically, physiologically, and histologically. New bone formation can be reinforced by using bioactive signals such as genes, tethered agents, soluble factors, total growth factor (TGF- $\beta$ ), and its subgroups such as bone morphogenetic protein (BMP) [8,9]. Protein adhesion initiates the initial phases of corrosion in human implants. Proteins either adhere permanently to metallic implants or depart from them through flow assisted by human bodily fluids, carrying some metallic fragments in the process. The disadvantage of conventional Ti-metallic implants is that it has strength ductility mismatch with bones and also release extra low interstitial (ELI) of Ti-6Al-4V leading to phosphorus deficiency in blood and bones [10].

To synthesize the HEA, a few basic parameters must be considered, including the Hume-Rothery rule [11,12], intrinsic properties such as entropy and enthalpy of mixing [13], valence electron configuration (VEC) [14], and rules for single phase, crystalline, intermetallic materials [3,15,16]. HEAs can be designed by evaluating the properties of materials that constitute HEA [17,18]. Alternatively, they can be synthesized by using computing techniques such as the phase-diagram calculation [19]. The principal equations that govern the properties of HEAs are as follows:

$$\Delta S_{mix} = R \sum_i^n c_i \ln c_i \quad (1)$$

$$VEC = \sum_{i=1}^n c_i (VEC)_i \quad (2)$$

$$\delta = 100\% \sqrt{\sum_{i=1}^n c_i \left(1 - \frac{r_i}{\sum_{j=1}^n c_j r_j}\right)^2} \quad (3)$$

$$\Delta H_{mix} = \sum_{i=1, i \neq j}^n \Omega_{ij} c_i c_j \quad (4)$$

$$\Omega = \frac{T_m \Delta S_{mix}}{|\Delta H_{mix}|} \quad (5)$$

where  $\Delta S_{mix}$  is the entropy of mixing,  $R$  is the universal gas constant,  $VEC$  denotes the valence electron configuration, delta ( $\delta$ ) is a unitless value indicating atomic size difference,  $\Delta H_{mix}$  is the enthalpy of mixing,  $\Omega$  is a dimensionless parameter that denotes energy gain,  $T_m$  is the melting point, and  $c_i$  is the atomic composition. These mathematical expressions are used to evaluate the alloy systems.

In conventional methods such as casting and powder metallurgy, samples must be recast and pressed several times under vacuum to achieve homogeneity [20]. Moreover, even after these processes, the elements do not mix with complete miscibility and form amalgamations in certain microscopic regions. By contrast, sputtering, a type of physical vapor deposition (PVD) method, involves more spontaneous mixing of the constituent materials. Moreover, it does not require additional recasting and pressing steps. With sputtering, the layer thickness of HEA, which impacts the corrosion resistance and biocompatibility of the underlying substrate, can be controlled easily. In this work, corrosion analyses of sputtered HEA thick and thin films in simulated body fluid (SBF) are performed, whereas in existing studies, the corrosion properties of HEA were studied in NaCl, H<sub>2</sub>SO<sub>4</sub>, and seawater. During sputtering, the films are subjected to a metastable-phase energy barrier of  $E \sim 0.25$  eV before their final adhesion to the substrate surface, and this metastable phase is the transition region between the gasification and substrate phases [21].

## 2. Materials and Methods

The top-down configuration of an Artec system magnetron sputtering machine was used for HEA deposition. This machine is equipped with a target holder measuring 4.25 in. The target holder was upgraded to accommodate 20 pieces. In total, six cobalt, two titanium, and four nickel, chromium, and molybdenum were cut by means of electron discharge machining (EDM). Approximately 99.99% pure elemental discs were procured

from THIFINE (the film and fine materials ©). To avoid charge accumulation at the target, the radiofrequency (RF) sputtering process was used, as illustrated in Figure 1a. The frequency ranged from 5 to 30 MHz, and the typical frequency was 13.56 MHz; electron densities ranged from  $10^9$  to  $10^{11}$   $\text{cm}^{-3}$ , and discharge pressure ranged from 0.5 to 10 mTorr [22]. Rare-earth magnets were used in the RF magnetron sputtering process. Figure 1b depicts how the magnetic field triggered a spiral momentum of the electrons around the target. This momentum increases the probability of sustained plasma, even at low pressures [23]. A  $5 \times 10^{-2}$  mbar vacuum was created before turning on the main valve (M/V). The samples were prepared at two different ion current densities of  $2 \times 10^{-5}$  A/cm<sup>2</sup> and  $5 \times 10^{-5}$  A/cm<sup>2</sup> [24]. Lower ion current densities reduce the likelihood of substrate oxidation [25]. After the thin HEA films were deposited by means of sputtering, the samples were post-treated in a multifunctional vacuum furnace (Ajeon Heating Industrial Co., Ltd., Namyangju-si, Republic of Korea) for 1 h at three different temperatures of 400 °C, 600 °C, and 800 °C. In this treatment, the maximum temperature was attained with a low heating curve rate, i.e., 5 °C per minute, to avoid large temperature gradients that result in tensile stresses and lead to the Kirkendall effect in coatings [26]. The treated samples were then cooled in a furnace under a 0.14 SCCM argon flow.

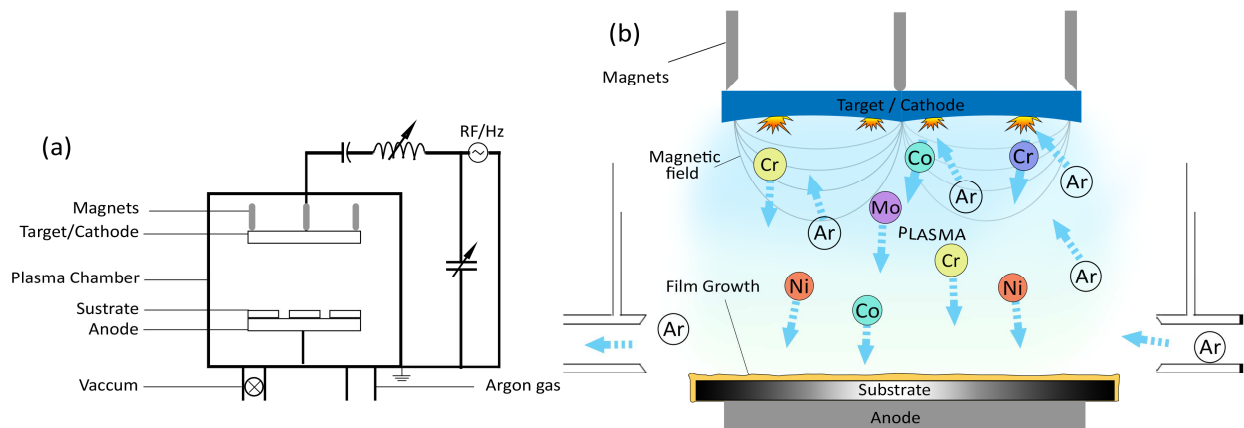


**Figure 1.** (a) Line diagram of radiofrequency (RF) magnetron sputtering; (b) Inside view of HEA sputtering process in the chamber.

Thermodynamic calculations were performed using mathematical expressions. From Equation (3), the average atomic radius  $r_{\text{avg}}$  of the prepared HEA  $\text{Co}_{30}\text{Cr}_{20}\text{Ni}_{20}\text{Mo}_{20}\text{Ti}_{10}$  was calculated as 1.2931 Å. The atomic size difference was 9.4%. By applying Equation (2) to the XPS composition analysis result of the sample (Table 1), the nominal valence electron configuration (VEC) was calculated as 7.15. The enthalpy of mixing was calculated using Equation (4) ( $\Delta H_{\text{mix}}$  was taken as  $-4.07$  kJ/mol) [27,28].

Corrosion experiments were conducted using BioLogic's VSP 300 potentiostat and EC-Lab software (v11.33). For corrosion testing, the Metek-designed flat cell K0235 was used, which exposes 1 cm<sup>2</sup> of the working electrode surface for greater accuracy. The cell was designed according to ASTM G5 with constant argon purging [29]. The fact that the oxygen in electrolytes reaches the surface of HEA affects the rate of oxidation on the HEA. By combining Fick's law for diffusion and Faraday's law, one can calculate the cathodic current associated with oxygen diffusion [30]. A simulated body fluid called Ringer's solution was selected as the electrolyte for corrosion testing, and Bode plots were constructed to analyze the electrochemical impedance of the synthesized HEA [31–34].

Cellular metabolic activities were monitored by developing a 3-(4,5-dimethylthiazol-2-yl)-2,5-diphenyl-2H-tetrazolium bromide (MTT) assay of osteoblast cell type (3T3 cells). MC 3T3 (osteoblast cells) were taken from a cryogenic freezer and grown in an incubator for one month in regular alpha-minimum essential medium (MEM) without L-ascorbic acid and phenol red at 37 °C and with 5% CO<sub>2</sub> supply. After the cells grew to 80% confluence in

a T-75 flask, they were sufficiently populated. Twice each week, the medium was changed, and the MTT assay was developed when the cell confluence exceeded  $1 \times 10^5$  cells/mL [35].

**Table 1.** Elemental composition and orbital configuration of deposited  $\text{Co}_{30}\text{Cr}_{20}\text{Ni}_{20}\text{Mo}_{20}\text{Ti}_{10}$  HEA.

Element	Atomic Percentage (%)	Binding Energy (eV)	FWHM ( $\Delta\text{eV}$ )	Chi-Square ( $\times 10^6$ )
Cobalt	31.89	777~794		
Co 2p <sub>3/2</sub>	80.41 of 31.89	778.42	1.10	3.25
Co 2p <sub>1/2</sub>	19.59 of 31.89	793.29	1.52	
Chromium	17.42	573~585		
Cr 2p <sub>3/2</sub>	74.20 of 17.42	574.46	1.77	5.74
Cr 2p <sub>1/2</sub>	25.80 of 17.42	583.58	1.75	
Molybdenum	21.93	227~231		
Mo 3d <sub>5/2</sub>	62.60 of 21.93	227.59	0.79	3.65
Mo 3d <sub>3/2</sub>	37.40 of 21.93	229.46	1.16	
Nickel	20.51	869~852		
Ni 2p <sub>3/2</sub>	62.24 of 20.51	852.70	1.29	4.08
Ni 2p <sub>3/2</sub>	7.29 of 20.51	859.60	2.46	
Ni 2p <sub>1/2</sub>	30.47 of 20.51	871.69	2.01	
Titanium	8.24	455~462		
Ti 2p <sub>3/2</sub>	59.52 of 8.24	455.02	1.50	0.34
Ti 2p <sub>1/2</sub>	40.48 of 8.24	461.67	1.83	

#### Thin-Film Characterization

X-ray diffraction analysis (XRD, using Cu-K radiation) was performed to examine the crystallinity and phase structure of the synthesized HEAs. A low scan rate ( $1^\circ/\text{min}$ ) was employed to obtain a higher resolution. The step size,  $2\theta$ , and omega range of the goniometer were  $0.02$ ,  $5\text{--}90^\circ$ , respectively, and a voltage of  $45\text{ kV}$  was used. By means of field-emission scanning electron microscopy, the thicknesses of the deposited thin films were measured (Model: Gemini 500). By using an Al  $K\alpha$  X-ray analyzer in conjunction with XPS (Model: K-ALPHA+) with a spot size of  $400\ \mu\text{m}$ , excitation energy of  $4.36\text{ keV}$ , energy step of  $0.05\text{ eV}$ , and pass energy of  $100\text{ eV}$ , the surface chemistries of the produced HEAs were determined. Argon etching was performed before characterization, and the C1 s peak was set to  $284.6\text{ eV}$ .

### 3. Results and Discussion

After sputtering with varying ion densities, SEM was used to determine the coating thickness, as shown in Figure 2. Higher ion density ( $5 \times 10^{-5}\text{ A/cm}^2$ ) had more argon ions inside the sputtering chamber, resulting in thicker samples (the samples synthesized by this parameter are called thick hereinafter), and samples prepared at low ion density, i.e.,  $2 \times 10^{-5}\text{ A/cm}^2$ , had less thickness with a difference of approximately  $250\text{ nm}$  w.r.t thick coating, labeled as thin hereinafter.

For XRD characterization, the amorphous peak of the thin films was absorbed because, according to Equation (3), the atomic difference of  $\text{Co}_{30}\text{Cr}_{20}\text{Ni}_{20}\text{Mo}_{20}\text{Ti}_{10}$  was  $5.57\%$ , which is in the amorphous region for HEAs, as depicted in Figure 3 [36].

The heat treatment temperature range was  $300\text{--}1000\text{ }^\circ\text{C}$  for the HEA without copper. In this temperature range, the compositional difference between the dendritic ends and the center was eliminated, except in the case of the HEAs with copper in them because, in this temperature range, copper tended to segregate [37]. So, the prepared HEAs were heat treated within given temperature ranges.

The lattice distortion effect of the HEA with varying atomic sizes led to a significant loss of crystallization, which simplified its XRD patterns at high temperatures and atypically lowered the peak heights of the (310) and (200) planes at  $600\text{ }^\circ\text{C}$  and  $800\text{ }^\circ\text{C}$ , respectively [36].

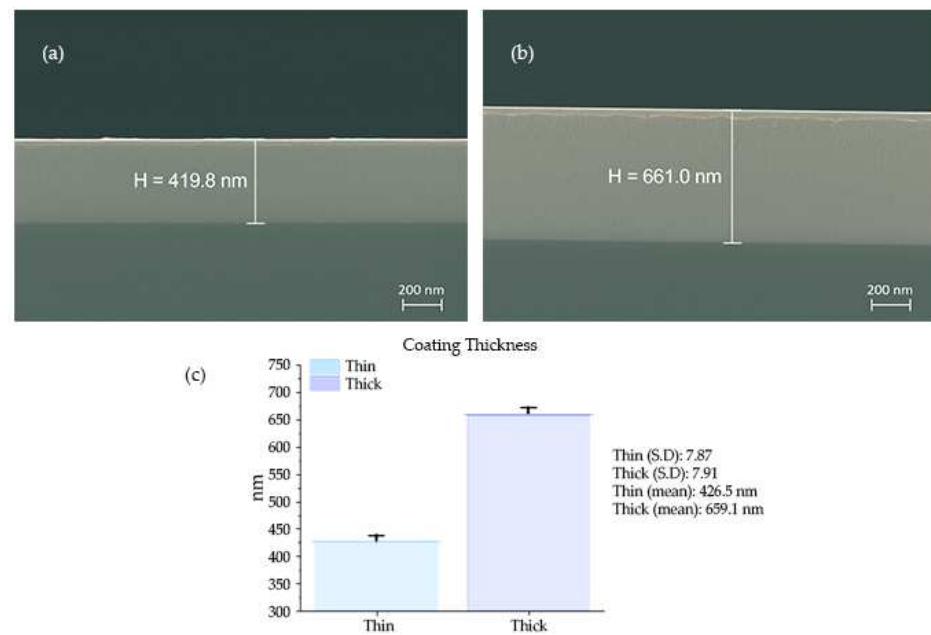


**Figure 2.** SEM analysis of HEA thin films synthesized at two different ion densities of (a)  $20 \mu\text{Acm}^{-2}$  (thin film) and (b)  $50 \mu\text{Acm}^{-2}$  (thick film). (c) Statistical differences between these two coatings.

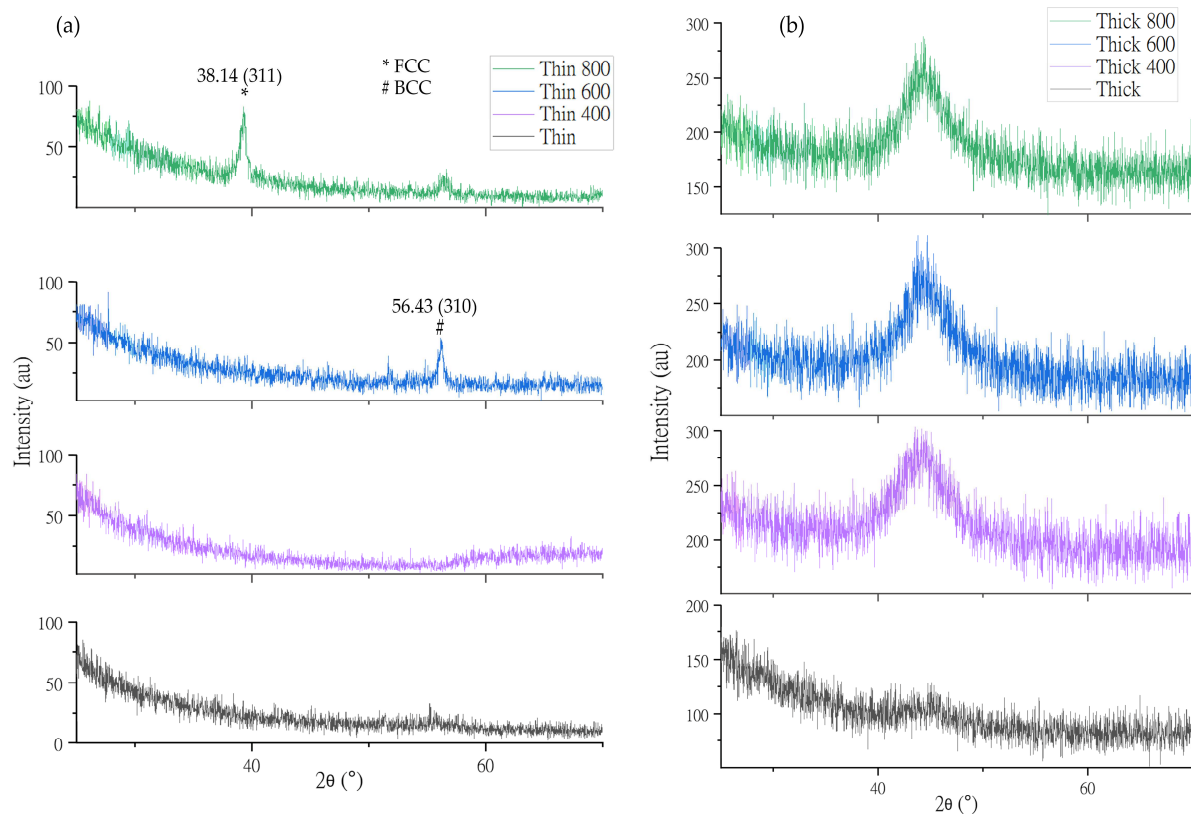


**Figure 3.** Amorphous XRD peaks of (a) thin and (b) thick HEA films without heat treatment (WHT) and heat treated at  $400^\circ\text{C}$ ,  $600^\circ\text{C}$ , and  $800^\circ\text{C}$ , respectively.

The XPS results of the alloy are depicted in Figure 4, along with the corresponding Gaussian peak fitting results. The XPS results were obtained using a sample that was not heat treated (Table 2) [38–42]. Figure 4a depicts the XPS survey spectrum, which confirms the coexistence of all deposited elements in the  $\text{Co}_{30}\text{Cr}_{20}\text{Ni}_{20}\text{Mo}_{20}\text{Ti}_{10}$  HEA. By means of Ar etching for 17 min before the XPS examination, we decreased the heights of the O1s

and C1s peaks considerably. Figure 4b depicts the XPS peaks of Cr at 574 eV and 583.5 eV, which correspond to Cr 2p<sub>3/2</sub> and Cr 2p<sub>1/2</sub>, respectively [41,43]. These peaks were further deconvoluted into two binding energies. In Figure 4c, cobalt has two prominent peaks at 778 and 793 eV, which correlate to Co2p<sub>3/2</sub> and Co2p<sub>1/2</sub>, respectively. These intensities are further split into two regions in each peak [39,44]. The peak at 230.8 eV corresponds to (Mo3d<sub>3/2</sub>) Mo<sup>+4</sup> [45] in Figure 4d, and in the same proximity, the peak centered at 227.5 eV corresponds to Mo3d<sub>5/2</sub> [38,40].

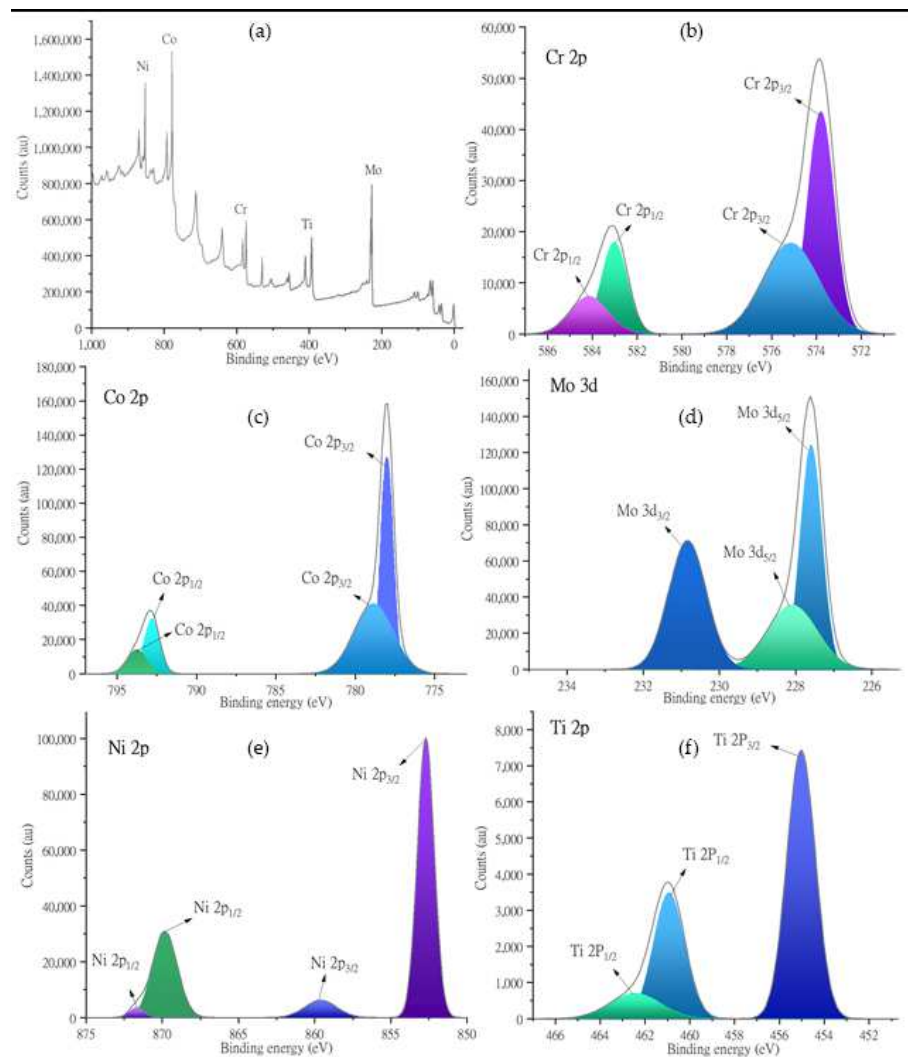


**Figure 4.** (a) XPS analysis of Co<sub>30</sub>Cr<sub>20</sub>Ni<sub>20</sub>Mo<sub>20</sub>Ti<sub>10</sub> HEA-synthesized through magnetron sputtering and the corresponding peak fitting of (b) chromium, (c) cobalt, (d) molybdenum, (e) nickel, and (f) titanium.

The nickel peaks in Figure 4e were discretized into Ni2p<sub>3/2</sub> peaks with spin-orbital characteristics at 852 and 859 eV and an Ni2p<sub>1/2</sub> peak centered at 870 eV [40,44]. Similarly in Figure 4f, the Ti peaks are split into a Ti2p<sub>3/2</sub> peak centered at 455 eV and two Ti2p<sub>1/2</sub> peaks centered at 461 eV [42].

The results of the XPS studies confirmed that Mo<sup>6+</sup> (Mo 3d<sub>5/2</sub>) and Mo<sup>4+</sup> (Mo 3d<sub>3/2</sub>) were present in the synthesized coatings, and these ions were an integral part of the passive Cr<sub>2</sub>O<sub>3</sub> films, in which Mo 3d<sub>5/2</sub> controlled the film stability. MoO<sub>4</sub><sup>2-</sup> and MoO<sub>2</sub> in these films, which had binding energies of around 227 eV and 230 eV, respectively, as listed in Table 1, acted as healers of any defects in the passive films [34].

**Table 2.** Electrochemical properties of HEA with reference to uncoated titanium CP-II.

Property	Uncoated	Thin Coat	Thin Coat 400	Thin Coat 600	Thin Coat 800	Thick Coat	Thick Coat 400	Thick Coat 600	Thick Coat 800
$E_{\text{corr}}$ (mV)	−363.08	−347.46	527.04	522.49	−318.95	−698.23	163.09	−297.67	−463.64
$I_{\text{corr}}$ ( $\mu\text{A}$ )	0.313	0.040	0.111	0.122	0.108	1.851	0.145	0.126	0.088
Corrosion rate (mmpy)	0.0108	0.0014	0.0038	0.0042	0.0037	0.0641	0.0050	0.0043	0.0030
Resistance ( $\Omega$ )	$1.16 \times 10^6$	$8.69 \times 10^6$	$4.74 \times 10^6$	$4.28 \times 10^6$	$2.96 \times 10^6$	$3.77 \times 10^5$	$1.12 \times 10^6$	$2.36 \times 10^6$	$5.26 \times 10^6$
$E_{\text{pit}}$ (V)	–	0.569			0.575	0.629	0.434		0.486
$\text{Log } I_{\text{pass}}$ (mA)	–	0.010			0.033	0.029	0.080		0.433

For corrosion analysis, the open-circuit potential was stabilized for 3 h, and polarization curves were drawn between  $-0.5$  V and  $1.5$  V at a scan rate of  $10$  mV/min on titanium (CP-II) substrate. The reference electrode for the electrochemical process was Ag/AgCl with 3M NaCl/saturated AgCl filling solution, and the electrode potential of the Ag/AgCl electrode is  $0.02$  V against the standard calomel electrode (SCE) [46]. The electrochemical impedance spectroscopy (EIS) experiment was run before drawing the Tafel plots in Figures 5 and 6 because EIS is a non-destructive analysis. Moreover, the electrochemical properties of the synthesized HEA are summarized in Table 2.

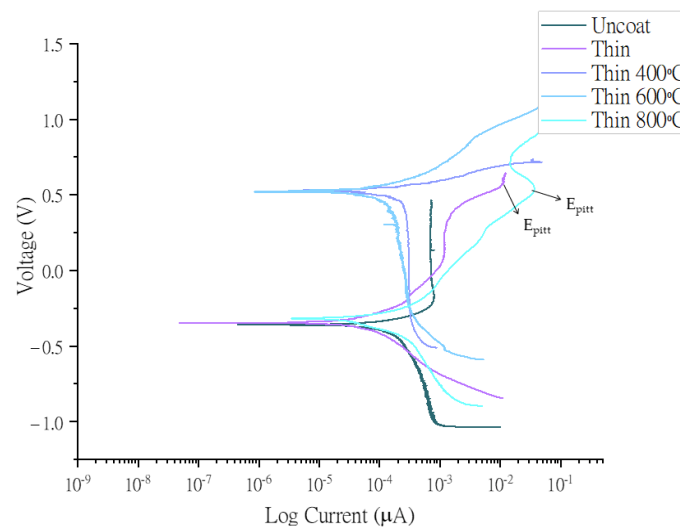


**Figure 5.** Polarization curves of Co30Cr20Ni20Mo20Ti10 alloy versus Ag/AgCl electrode in Hank's solution. Working electrode was deposited at  $2 \times 10^5$  ion density (thin coat) without heat treatment and with heat treatment at  $400$  °C,  $600$  °C, and  $800$  °C.

As a biomaterial, the synthesized HEA surface coating must be characterized electrochemically to understand its behavior on implants from the perspective of avoiding inflammation through the release of ions into the human body. This is because the synergic effect of HEA and its corrosion characteristics vary significantly from those of known electrochemical processes.

The pitting corrosion on the coating surface is considered a major disadvantage for biomedical implants. In the discussion of the corrosion, we can add the fact that in the trans-passive region of the potentiodynamic curve, potential considerably greater than the corrosion potential pitting occurs (ref: ASTM-F746-0), as illustrated in Figures 5 and 6.

The uncoated sample was a substrate of commercially pure titanium grade II substrate. The polarization curves represented in Figures 5 and 6 were measured against the open-circuit potential. Ag/AgCl, and a Pt mesh were used as a reference and counter electrodes, respectively. Table 2 lists the current densities, corrosion resistance, and other important values obtained from the Tafel plots after fitting in EC-Lab software.

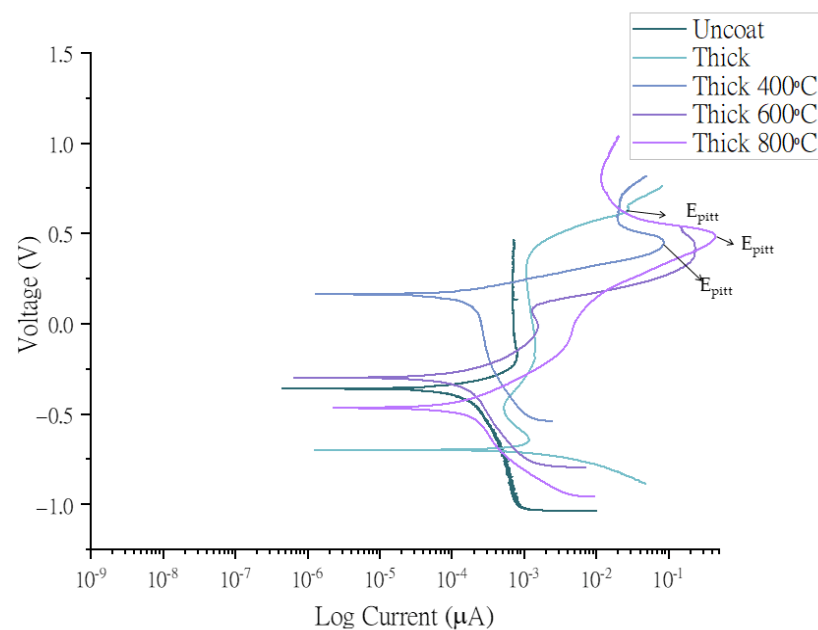


**Figure 6.** Polarization curves of Co<sub>30</sub>Cr<sub>20</sub>Ni<sub>20</sub>Mo<sub>20</sub>Ti<sub>10</sub> alloy versus Ag/AgCl electrode in Hank's solution. Working electrode was deposited at  $5 \times 10^5$  ion density (thin coat) without heat treatment and with heat treatment at 400 °C, 600 °C, and 800 °C.

The atomic arrangement of synthesized HEA was amorphous, and high temperature leads to thermally active movement of atoms resulting in the formation of a small-ordered crystal structure, as depicted in Figure 3. Due to this movement, the compactibility of the coating is compromised, resulting in high current densities at elevated temperatures [47], as shown in Table 2. In the synthesized thin film, Mo-O and Cr-O generate a passivation mechanism by providing a healing effect to the coating. Therefore the amounts of molybdenum and chromium in the coating gives a passivation mechanism by the Cr-rich sigma ( $\sigma$ ) phase [16]. This is corroborated by the high corrosion resistance of  $8.69 \times 10^9 \Omega$  of the thin film [34]. Cr (VI) is released from an alloy. It is only present for a very limited time because it is quickly reduced to the trivalent state in vivo [48].

Electrochemical impedance is a measurement of the resistance of coating for a given frequency and phase of alternating current. The higher the potential of a material, the lower its electron density at that potential, which means that there is more space for electrons to flow, and the surface is therefore resistant to oxidation. Electrochemical impedance characterization was performed by analyzing the Bode plots of the samples, as depicted in Figure 7. The frequency range used for the EIS measurements was 10 kHz to 1 mHz, and 1 sinusoidal wave was composed of 10 nodes of data points. Constant phase elements (CPEs) were determined using the following equation.

$$Z_{CPE}(\omega) = \omega \frac{1}{(i\omega)^\alpha Q} \quad (6)$$

where  $\omega$  is the angular frequency  $0 \leq \alpha \leq 1$ . At higher and lower frequencies, the circuit acted as capacitive and resistive, respectively.

The Bode plots show the variation of the impedance modulus and the phase angle of the CPEs in the film at the applied frequency of the sinusoidal signal. HEAs have higher impedance owing to the presence of metals that generate more ions in the resistive region, that is, at low frequencies ranging from  $10^{-2}$  to  $10^{-1}$ , the thick and thin 400 °C samples show less contribution of charge transfer because their magnitudes are greater than  $10^2$  to  $10^3 \Omega$  on a logarithmic scale.

MTT dye was analyzed using a wavelength of 570 nm to perform a cell viability analysis. Osteoblast 3T3 cells were grown on processed Co<sub>30</sub>Cr<sub>20</sub>Ni<sub>20</sub>Mo<sub>20</sub>Ti<sub>10</sub> HEAs, and

their compatibility is shown in Figure 8. MTT analysis was performed at a significance level of 0.05 and a mean square value of 0.16. The sample heat treated at 600 °C indicated a significant difference in variability ( $S = 0.05$ ). This HEA sample contained 10% Ti in three structural forms, namely alpha, beta, and alpha-beta phases, depending on the heat treatment condition and alloying additions. At 600 °C, the Ti was mostly  $\alpha$ -Ti, leading to reduced cell viability [49]. Mo and Cr also functioned as beta stabilizers, for instance, in ASTM F 2066. Moreover, the biocompatibility of the samples decreased as their heat treatment temperature increased, as the electrical current started to flow within the cells [50]. The samples heat treated at 800 °C exhibited little crystallinity in the XRD (Figure 3), and accordingly, their biocompatibility was poor.

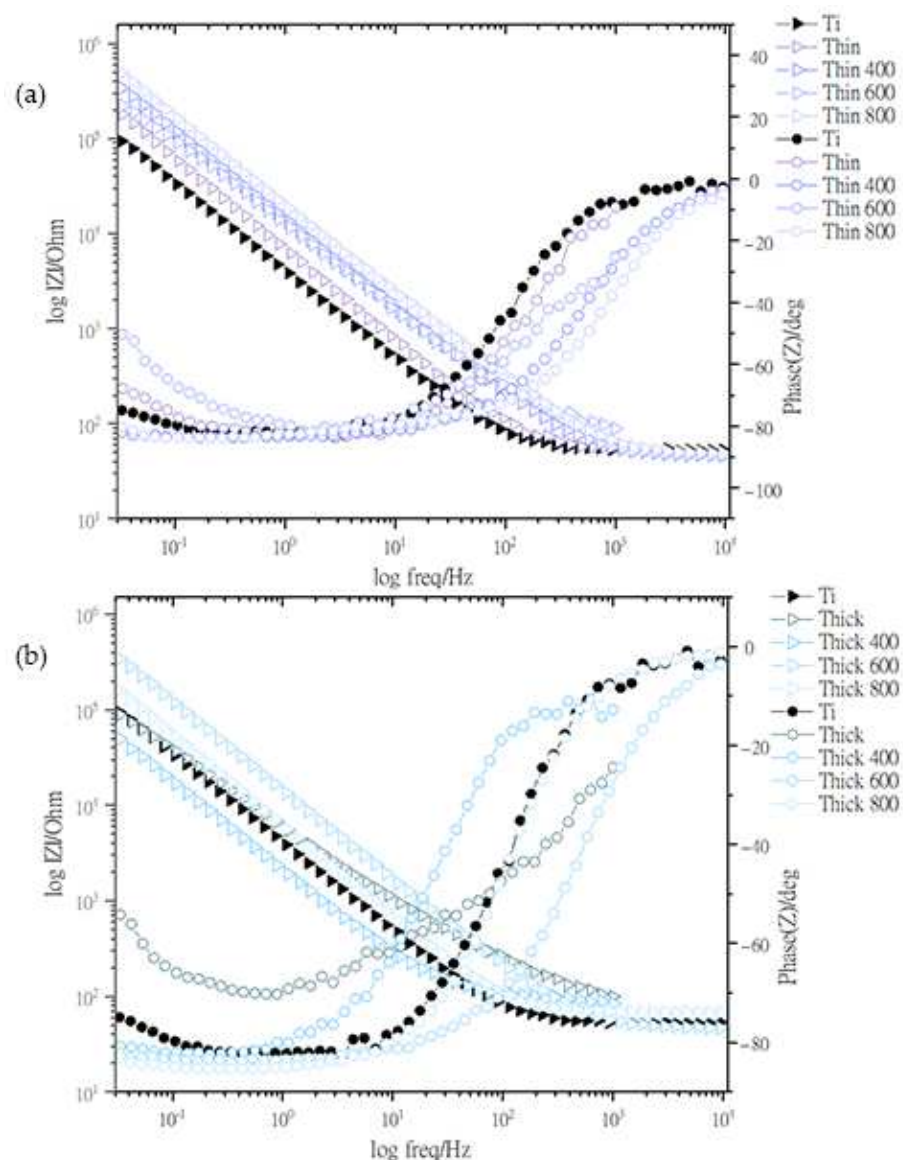


**Figure 7.** Impedance plots (Bode curve) of  $\text{Co}_{30}\text{Cr}_{20}\text{Ni}_{20}\text{Mo}_{20}\text{Ti}_{10}$  alloy versus Ag/AgCl electrode in Hank's solution. Working electrode was deposited at (a)  $2 \times 10^5$  ion density (thin coat) without heat treatment and with heat treatment at 400 °C, 600 °C, and 800 °C (b); (a)  $5 \times 10^5$  ion density (thin coat) without heat treatment and with heat treatment at 400 °C, 600 °C, and 800 °C.

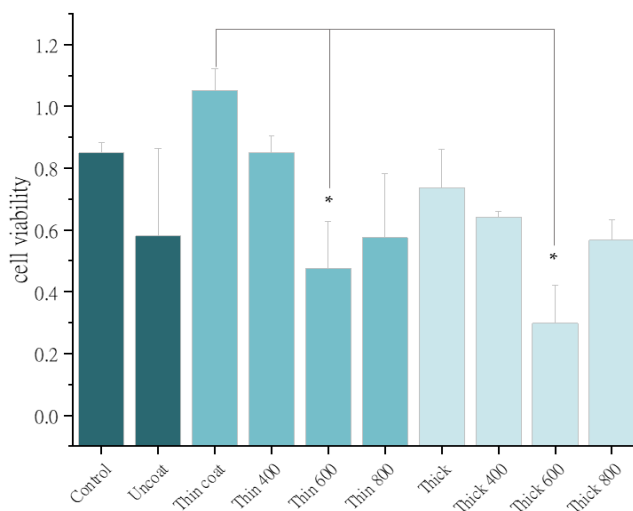


**Figure 8.** MTT analysis of uncoated titanium surface, coated  $\text{Co}_{30}\text{Cr}_{20}\text{Ni}_{20}\text{Mo}_{20}$ , and heat treated surfaces. The significant difference between thin coat and samples heat treated at 600 °C is marked with hysteric.

**4. Conclusions**

In this work, the thin HEA coating of 419 nm produced by sputtering at  $2 \times 10^{-5} \text{ A/cm}^2$  ion density and without heat treatment outperformed all the other samples in terms of corrosion resistance of  $8.69 \times 10^6 \Omega\text{-cm}^2$  (Table 2) and biological cell viability (Figure 8). In our analysis, we studied an HEA by considering two variables, namely coating thickness in nanoscale and heat treatment temperature. In our analysis of the EIS property of the deposited HEA thin films, the WHT thin film formed a resistive circuit that protected biological cells and allowed current flow in the extracellular region. Therefore, this coating must have had a compacted passive layer. If the chromium content of the HEA exceeded 12%, molybdenum eliminated hydroxide ions from chromium. Similarly, nickel and cobalt enhanced the strength of the passivation layer, which increased its resistance to pitting corrosion [51], as shown in Table 2 [34]. The samples coated with  $\text{Co}_{30}\text{Cr}_{20}\text{Ni}_{20}\text{Mo}_{20}\text{Ti}_{10}$  at low ion density and without heat treatment produced relatively good osteoblast cell viability and corrosion resistance, as illustrated in Figure 9. This finding is solely attributable to the fact that coated samples tend to have less structure distortion than the other samples, and atomic mobility is noticeable in the XRD results from the remaining samples.

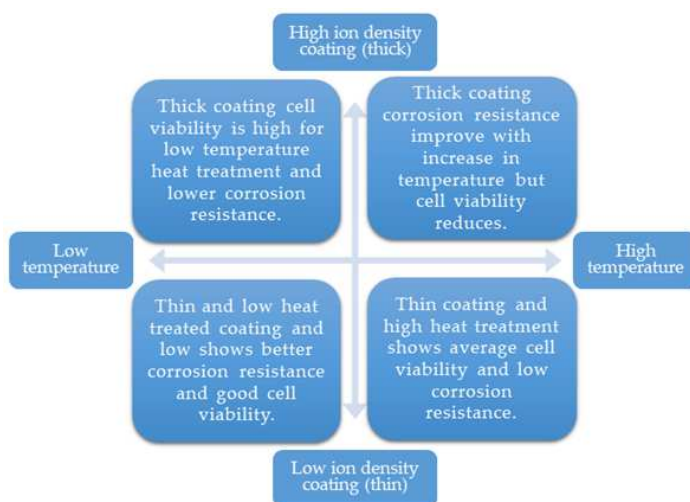


**Figure 9.** Effect of heat treatment and coating thickness on electrochemical property and osteoblastic cell viability.

**Author Contributions:** Conceptualization, K.A. and H.C.; Methodology, K.U. and G.J.; Software, D.K.; Validation, G.J., K.A., A.R. and J.S.; Formal analysis, K.U., K.A. and J.S.; Investigation, D.K. and A.R.; Resources, A.R.; Data curation, G.J.; Writing—original draft, K.U. and D.K.; Writing—review & editing, J.S. and W.J.; Visualization, K.U.; Supervision, H.C.; Project administration, W.J. and H.C.; Funding acquisition, W.J. and H.C. All authors have read and agreed to the published version of the manuscript.

**Funding:** This work was supported by a National Research Foundation of Korea (NRF) grant funded by the Korea Government (MSIT) (No. 2021R1F1A1064062) and by the Basic Science Research Program through the National Research Foundation of Korea (NRF) funded by the Ministry of Education (No. 2021R1I1A1A01058691).

**Institutional Review Board Statement:** Not applicable.

**Informed Consent Statement:** Not applicable.

**Data Availability Statement:** Data will be available upon request.

**Conflicts of Interest:** This research article has no conflict of interest. The authors declare that they have no conflicts of interest related to the content of this work.

## References

1. Yeh, J.-W.; Chen, S.K.; Lin, S.-J.; Gan, J.-Y.; Chin, T.-S.; Shun, T.-T.; Tsau, C.-H.; Chang, S.-Y. Nanostructured High-Entropy Alloys with Multiple Principal Elements: Novel Alloy Design Concepts and Outcomes. *Adv. Eng. Mater.* **2004**, *6*, 299–303. [\[CrossRef\]](#)
2. Cantor, B.; Chang, I.T.H.; Knight, P.; Vincent, A.J.B. Microstructural development in equiatomic multicomponent alloys. *Mater. Sci. Eng. A* **2004**, *375*, 213–218. [\[CrossRef\]](#)
3. George, E.P.; Raabe, D.; Ritchie, R.O. High-Entropy Alloys. *Nat. Rev. Mater.* **2019**, *4*, 515–534. [\[CrossRef\]](#)
4. Geib, F.W. Vitallium Skull Plates. *J. Am. Med. Assoc.* **1941**, *117*, 8–12. [\[CrossRef\]](#)
5. Alvi, S.; Jarzabek, D.M.; Kohan, M.G.; Hedman, D.; Jenczyk, P.; Natile, M.M.; Vomiero, A.; Akhtar, F. Synthesis and Mechanical Characterization of a CuMoTaWV High-Entropy Film by Magnetron Sputtering. *ACS Appl. Mater. Interfaces* **2020**, *12*, 21070–21079. [\[CrossRef\]](#)
6. Vaicelyte, A.; Janssen, C.; Le Borgne, M.; Grosgeat, B. Cobalt–Chromium Dental Alloys: Metal Exposures, Toxicological Risks, CMR Classification, and EU Regulatory Framework. *Crystals* **2020**, *10*, 1151. [\[CrossRef\]](#)
7. Linauskienė, K.; Malinauskienė, L.; Blažienė, A. Metals Are Important Contact Sensitizers: An Experience from Lithuania. *BioMed Res. Int.* **2017**, *2017*, 3964045. [\[CrossRef\]](#)
8. Ring, P.A. Complete Replacement Arthroplasty of the Hip by the Ring Prosthesis. *J. Bone Jt. Surg. Br. Vol.* **1968**, *50*, 720–731. [\[CrossRef\]](#)
9. Paralkar, V.M.; Grasser, W.A.; Riccardi, K.A.; Thompson, D.D.; Vukicevic, S. *Bone Healing Bone Morphogenetic Proteins and Beyond, in Bone Morphogenetic Proteins: Regeneration of Bone and Beyond*; Vukicevic, S., Sampath, K.T., Eds.; Birkhäuser Basel: Basel, Switzerland, 2004; pp. 293–305.
10. Gurappa, I. Characterization of different materials for corrosion resistance under simulated body fluid conditions. *Mater. Charact.* **2002**, *49*, 73–79. [\[CrossRef\]](#)
11. Mizutani, U. *Hume-Rothery Rules for Structurally Complex Alloy Phases*; Tylor & Francis Group: Boca Raton, FL, USA, 2010; p. 356.
12. Pei, Z.; Yin, J.; Hawk, J.A.; Alman, D.E.; Gao, M.C. Machine-learning informed prediction of high-entropy solid solution formation: Beyond the Hume-Rothery rules. *npj Comput. Mater.* **2020**, *6*, 50. [\[CrossRef\]](#)
13. Otto, F.; Yang, Y.; Bei, H.; George, E. Relative effects of enthalpy and entropy on the phase stability of equiatomic high-entropy alloys. *Acta Mater.* **2013**, *61*, 2628–2638. [\[CrossRef\]](#)
14. Chen, R.; Qin, G.; Zheng, H.; Wang, L.; Su, Y.; Chiu, Y.; Ding, H.; Guo, J.; Fu, H. Composition design of high entropy alloys using the valence electron concentration to balance strength and ductility. *Acta Mater.* **2018**, *144*, 129–137. [\[CrossRef\]](#)
15. Tsai, M.-H.; Yeh, J.-W. High-Entropy Alloys: A Critical Review. *Mater. Res. Lett.* **2014**, *2*, 107–123. [\[CrossRef\]](#)
16. Qiu, Y.; Thomas, S.; Gibson, M.A.; Fraser, H.L.; Birbilis, N. Corrosion of high entropy alloys. *npj Mater. Degrad.* **2017**, *1*, 15. [\[CrossRef\]](#)
17. Ye, Y.; Wang, Q.; Lu, J.; Liu, C.; Yang, Y. High-entropy alloy: Challenges and prospects. *Mater. Today* **2016**, *19*, 349–362. [\[CrossRef\]](#)
18. Pei, Z.; Yin, J.; Liaw, P.K.; Raabe, D. Toward the design of ultrahigh-entropy alloys via mining six million texts. *Nat. Commun.* **2023**, *14*, 54. [\[CrossRef\]](#)
19. George, E.P.; Curtin, W.A.; Tasan, C.C. High entropy alloys: A focused review of mechanical properties and deformation mechanisms. *Acta Mater.* **2020**, *188*, 435–474. [\[CrossRef\]](#)
20. Song, H.; Lee, S.; Lee, K. Thermodynamic parameters, microstructure, and electrochemical properties of equiatomic TiMoVWCr and TiMoVNbZr high-entropy alloys prepared by vacuum arc remelting. *Int. J. Refract. Met. Hard Mater.* **2021**, *99*, 105595. [\[CrossRef\]](#)
21. Ohring, M. Chapter 7—Substrate Surfaces and Thin-Film Nucleation. In *Materials Science of Thin Films*, 2nd ed.; Ohring, M., Ed.; Academic Press: San Diego, CA, USA, 2002; pp. 357–415.

22. Mattox, D.M. Chapter 7—Physical Sputtering and Sputter Deposition (Sputtering). In *Handbook of Physical Vapor Deposition (PVD) Processing*, 2nd ed.; Mattox, D.M., Ed.; William Andrew Publishing: Boston, MA, USA, 2010; pp. 237–286.
23. Ohring, M. Chapter 5—Plasma and Ion Beam Processing of Thin Films. In *Materials Science of Thin Films*, 2nd ed.; Ohring, M., Ed.; Academic Press: San Diego, CA, USA, 2002; pp. 203–275.
24. Morris, A.; Langari, R. *Measurement and Instrumentation: Theory and Application*; Butterworth-Heinemann: Oxford, UK, 2012.
25. Xing, Q.; Wang, H.; Chen, M.; Chen, Z.; Li, R.; Jin, P.; Zhang, Y. Mechanical Properties and Corrosion Resistance of NbTiAlSiZrNx High-Entropy Films Prepared by RF Magnetron Sputtering. *Entropy* **2019**, *21*, 396. [[CrossRef](#)]
26. Song, B.; Yang, Y.; Rabbani, M.; Yang, T.T.; He, K.; Hu, X.; Yuan, Y.; Ghildiyal, P.; Dravid, V.P.; Zachariah, M.R.; et al. In Situ Oxidation Studies of High-Entropy Alloy Nanoparticles. *ACS Nano* **2020**, *14*, 15131–15143. [[CrossRef](#)]
27. Guo, S.; Liu, C.T. Phase stability in high entropy alloys: Formation of solid-solution phase or amorphous phase. *Prog. Nat. Sci. Mater. Int.* **2011**, *21*, 433–446. [[CrossRef](#)]
28. Takeuchi, A.; Inoue, A. Classification of Bulk Metallic Glasses by Atomic Size Difference, Heat of Mixing and Period of Constituent Elements and Its Application to Characterization of the Main Alloying Element. *Mater. Trans.* **2005**, *46*, 2817–2829. [[CrossRef](#)]
29. Kinetics: Polarization and Corrosion Rates. In *Corrosion and Corrosion Control*; John Wiley & Sons: Hoboken, NJ, USA, 2008; pp. 53–82.
30. Scheiner, S.; Hellmich, C. Finite Volume model for diffusion- and activation-controlled pitting corrosion of stainless steel. *Comput. Methods Appl. Mech. Eng.* **2009**, *198*, 2898–2910. [[CrossRef](#)]
31. Manam, N.S.; Harun, W.S.W.; Shri, D.N.A.; Ghani, S.A.C.; Kurniawan, T.; Ismail, M.H.; Ibrahim, M.H.I. Study of corrosion in biocompatible metals for implants: A review. *J. Alloys Compd.* **2017**, *701*, 698–715. [[CrossRef](#)]
32. Vidal, C.V.; Muñoz, A.I. Electrochemical characterisation of biomedical alloys for surgical implants in simulated body fluids. *Corros. Sci.* **2008**, *50*, 1954–1961. [[CrossRef](#)]
33. Metikoš-Huković, M.; Katić, J.; Grubač, Z.; Škugor Rončević, I. Electrochemistry of CoCrMo Implant in Hanks' Solution and Mott-Schottky Probe of Alloy's Passive Films. *Corrosion* **2017**, *73*, 1401–1412. [[CrossRef](#)]
34. Karri, M.; Verma, A.; Singh, J.; Bonagani, S.K.; Goutam, U. Role of Chromium in Anomalous Behavior of the Passive Layer in Ni-Cr-Mo Alloys in 1 M HCl Solution. *Corrosion* **2022**, *78*, 228–238. [[CrossRef](#)]
35. Zebisch, K.; Voigt, V.; Wabitsch, M.; Brandsch, M. Protocol for effective differentiation of 3T3-L1 cells to adipocytes. *Anal. Biochem.* **2012**, *425*, 88–90. [[CrossRef](#)]
36. Yeh, J.W.; Chang, S.Y.; Hong, Y.D.; Chen, S.K.; Lin, S.J. Anomalous decrease in X-ray diffraction intensities of Cu–Ni–Al–Co–Cr–Fe–Si alloy systems with multi-principal elements. *Mater. Chem. Phys.* **2007**, *103*, 41–46. [[CrossRef](#)]
37. Li, Y.J.; Savan, A.; Kostka, A.; Stein, H.S.; Ludwig, A. Accelerated atomic-scale exploration of phase evolution in compositionally complex materials. *Mater. Horiz.* **2018**, *5*, 86–92. [[CrossRef](#)]
38. Kang, N.; Paudel, H.P.; Leuenberger, M.N.; Tetard, L.; Khondaker, S.I. Photoluminescence Quenching in Single-Layer MoS<sub>2</sub> via Oxygen Plasma Treatment. *J. Phys. Chem. C* **2014**, *118*, 21258–21263. [[CrossRef](#)]
39. Jacobs, G.; Chaney, J.A.; Patterson, P.M.; Das, T.K.; Davis, B.H. Fischer–Tropsch synthesis: Study of the promotion of Re on the reduction property of Co/Al<sub>2</sub>O<sub>3</sub> catalysts by in situ EXAFS/XANES of Co K and Re LIII edges and XPS. *Appl. Catal. A Gen.* **2004**, *264*, 203–212. [[CrossRef](#)]
40. Hong, S.T.; Park, D.R.; Yoo, S.-J.; Kim, J.-D.; Park, H.S. Characterization of the active phase of NiMo/Al<sub>2</sub>O<sub>3</sub> hydrodesulfurization catalysts. *Res. Chem. Intermed.* **2006**, *32*, 857–870. [[CrossRef](#)]
41. Harrison, P.G.; Lloyd, N.C.; Daniell, W. The Nature of the Chromium Species Formed during the Thermal Activation of Chromium-Promoted Tin(IV) Oxide Catalysts: An EPR and XPS Study. *J. Phys. Chem. B* **1998**, *102*, 10672–10679. [[CrossRef](#)]
42. Atuchin, V.V.; Kesler, V.G.; Pervukhina, N.V.; Zhang, Z. Ti 2p and O 1s core levels and chemical bonding in titanium-bearing oxides. *J. Electron Spectrosc. Relat. Phenom.* **2006**, *152*, 18–24. [[CrossRef](#)]
43. Bumajdad, A.; Al-Ghareeb, S.; Madkour, M.; Sagheer, F.A. Non-noble, efficient catalyst of unsupported  $\alpha$ -Cr<sub>2</sub>O<sub>3</sub> nanoparticles for low temperature CO Oxidation. *Sci. Rep.* **2017**, *7*, 14788. [[CrossRef](#)]
44. Yang, X.; Wang, H.; Song, Y.; Liu, K.; Huang, T.; Wang, X.; Zhang, C.; Li, J. Low-Temperature Synthesis of a Porous High-Entropy Transition-Metal Oxide as an Anode for High-Performance Lithium-Ion Batteries. *ACS Appl. Mater. Interfaces* **2022**, *14*, 26873–26881. [[CrossRef](#)]
45. Chua, X.J.; Pumera, M. Molybdenum Sulfide Electrocatalysis is Dramatically Influenced by Solvents Used for Its Dispersions. *ACS Omega* **2018**, *3*, 14371–14379. [[CrossRef](#)]
46. Resnik, D.; Pecar, B.; Mozek, M.; Lokar, N.; Vrtacnik, D. Formation of thin film Ag/AgCl reference electrode by electrochemical and chemical method. In Proceedings of the 2019 42nd International Convention on Information and Communication Technology, Electronics and Microelectronics (MIPRO), Opatija, Croatia, 20–24 May 2019.
47. Oje, A.M.; Ogwu, A.A. Chromium oxide coatings with the potential for eliminating the risk of chromium ion release in orthopaedic implants. *R. Soc. Open Sci.* **2017**, *4*, 170218. [[CrossRef](#)]
48. Meek, R.M.; Afolaranmi, G.A.; Tettey, J.; Grant, M.H. Release of chromium from orthopaedic arthroplasties. *Open Orthop. J.* **2008**, *2*, 10–18. [[CrossRef](#)]
49. Eisenbarth, E.; Velten, D.; Müller, M.; Thull, R.; Breme, J. Biocompatibility of  $\beta$ -stabilizing elements of titanium alloys. *Biomaterials* **2004**, *25*, 5705–5713. [[CrossRef](#)] [[PubMed](#)]

50. Bera, T.K. Bioelectrical Impedance and the Frequency Dependent Current Conduction through Biological Tissues: A Short Review. *IOP Conf. Ser. Mater. Sci. Eng.* **2018**, *331*, 012005. [[CrossRef](#)]
51. Fu, Y.; Li, J.; Luo, H.; Du, C.; Li, X. Recent advances on environmental corrosion behavior and mechanism of high-entropy alloys. *J. Mater. Sci. Technol.* **2021**, *80*, 217–233. [[CrossRef](#)]

**Disclaimer/Publisher's Note:** The statements, opinions and data contained in all publications are solely those of the individual author(s) and contributor(s) and not of MDPI and/or the editor(s). MDPI and/or the editor(s) disclaim responsibility for any injury to people or property resulting from any ideas, methods, instructions or products referred to in the content.